nature portfolio

https://doi.org/10.1038/s41586-023-06911-x

Supplementary information

Observing dynamical phases of BCS superconductors in a cavity QED simulator

In the format provided by the authors and unedited

Observing Dynamical Phases of BCS Superconductors in a Cavity QED Simulator: Supplemental Materials

Dylan J. Young,[1,*] Anjun Chu,[1,2,*] Eric Yilun Song,[1] Diego Barberena,[1,2] David Wellnitz,[1,2] Zhijing Niu,[1] Vera M. Schäfer,[1,3] Robert J. Lewis-Swan,[4,5] Ana Maria Rey,[1,2] and James K. Thompson[1]

[1] *JILA, NIST, and Department of Physics, University of Colorado, Boulder, CO, USA*
[2] *Center for Theory of Quantum Matter, University of Colorado, Boulder, CO, USA*
[3] *Max-Planck-Institut für Kernphysik, Saupfercheckweg 1, 69117 Heidelberg, Germany*
[4] *Homer L. Dodge Department of Physics and Astronomy, University of Oklahoma, Norman, OK, USA*
[5] *Center for Quantum Research and Technology, University of Oklahoma, Norman, OK, USA*

(Dated: November 13, 2023)

S1. DYNAMICAL PHASE DIAGRAM

In this section, we perform detailed analysis of the dynamical phase diagram shown in Fig. 1**c** in the main text. We start from analytic calculation in the case of homogeneous couplings, and then generalize to the case of inhomogeneous couplings. Finally we discuss the application of our findings to experimental conditions.

A. Homogeneous model

First we discuss the dynamical phases for the BCS Hamiltonian with homogeneous couplings,

$$\hat{H} = \hbar\chi\hat{S}^{+}\hat{S}^{-} + \sum_{k}\varepsilon_{k}\hat{S}^{z}_{k}. \tag{S1}$$

We will set $\hbar = 1$. As shown in Ref. [**? ?**], the dynamical phases can be determined using a mean-field Lax vector analysis. The Lax vector is defined as $\vec{L}(u) = L^{x}(u)\hat{x} + L^{y}(u)\hat{y} + L^{z}(u)\hat{z}$ with components,

$$L^{x}(u) = \sum_{k}\frac{S^{x}_{k}(0)}{u-\varepsilon_{k}/2}, \quad L^{y}(u) = \sum_{k}\frac{S^{y}_{k}(0)}{u-\varepsilon_{k}/2}, \quad L^{z}(u) = -\frac{1}{\chi} - \sum_{i}\frac{S^{z}_{k}(0)}{u-\varepsilon_{k}/2}, \tag{S2}$$

where $S^{x,y,z}_{k}(0)$ are the expectation value of operators $\hat{S}^{x,y,z}_{k}$ in the initial state.

Here we consider the initial state as $S^{x}_{k}(0) = 1/2$, $S^{y}_{k}(0) = S^{z}_{k}(0) = 0$, and ε_{k} is chosen from a uniform distribution in the frequency range $[-\delta_{\mathrm{s}}/2 - E_{\mathrm{W}}/2, -\delta_{\mathrm{s}}/2 + E_{\mathrm{W}}/2]$ and $[\delta_{\mathrm{s}}/2 - E_{\mathrm{W}}/2, \delta_{\mathrm{s}}/2 + E_{\mathrm{W}}/2]$. In this case, the mean-field Lax vector takes the following form:

$$\begin{aligned}
\chi L^{x}(u) &\approx \frac{\chi N}{2}\left[\frac{1}{2E_{\mathrm{W}}}\int_{-\delta_{\mathrm{s}}/2-E_{\mathrm{W}}/2}^{-\delta_{\mathrm{s}}/2+E_{\mathrm{W}}/2}\frac{dx}{u-x/2} + \frac{1}{2E_{\mathrm{W}}}\int_{\delta_{\mathrm{s}}/2-E_{\mathrm{W}}/2}^{\delta_{\mathrm{s}}/2+E_{\mathrm{W}}/2}\frac{dx}{u-x/2}\right] \\
&= \frac{\chi N}{2E_{\mathrm{W}}}\left[\ln\left(u+\frac{\delta_{\mathrm{s}}}{4}+\frac{E_{\mathrm{W}}}{4}\right) - \ln\left(u+\frac{\delta_{\mathrm{s}}}{4}-\frac{E_{\mathrm{W}}}{4}\right) + \ln\left(u-\frac{\delta_{\mathrm{s}}}{4}+\frac{E_{\mathrm{W}}}{4}\right) - \ln\left(u-\frac{\delta_{\mathrm{s}}}{4}-\frac{E_{\mathrm{W}}}{4}\right)\right], \\
&\chi L^{y}(u) = 0, \\
&\chi L^{z}(u) = -1.
\end{aligned} \tag{S3}$$

Note that $\ln z$ in the complex plane is a multivalued function. Here we take the principal value $\ln z = \ln|z| + i\mathrm{Arg}(z)$, where $\mathrm{Arg}(z)$ is the argument of z restricted in the interval $(-\pi, \pi]$. Directly combining the logarithm functions might lead to moving out of the principal branch.

One can define the dynamical phases based on the number of complex roots of equation $\vec{L}(u)\cdot\vec{L}(u) = 0$: Phase I has zero complex roots, phase II has a pair of complex roots, phase III has two pairs of complex roots. Whether the

---

* These authors contributed equally to this work.

complex roots have non-zero or vanishing real parts could be used for further separation of the phases. In our case, the equation $\vec{L}(u)\cdot\vec{L}(u)=0$ takes the following form,

$$\frac{\chi N}{2E_{\rm W}}\left[\ln\left(u+\frac{\delta_{\rm s}}{4}+\frac{E_{\rm W}}{4}\right)-\ln\left(u+\frac{\delta_{\rm s}}{4}-\frac{E_{\rm W}}{4}\right)+\ln\left(u-\frac{\delta_{\rm s}}{4}+\frac{E_{\rm W}}{4}\right)-\ln\left(u-\frac{\delta_{\rm s}}{4}-\frac{E_{\rm W}}{4}\right)\right]=\pm i. \tag{S4}$$

We find four dynamical phases based on analyzing the roots of Eq. (S4):

- Phase I: No complex roots, which exist in the regime

$$\frac{\delta_{\rm s}}{E_{\rm W}}<1,\quad \frac{\chi N}{E_{\rm W}}<\frac{1}{\pi}\qquad\text{or}\qquad \frac{\delta_{\rm s}}{E_{\rm W}}>1,\quad \frac{\chi N}{E_{\rm W}}<\frac{2}{\pi}. \tag{S5}$$

- Phase II: A pair of complex roots,

$$\frac{u}{E_{\rm W}}=\pm\frac{i}{4}\left[\cot\left(\frac{E_{\rm W}}{\chi N}\right)+\sqrt{\csc^2\left(\frac{E_{\rm W}}{\chi N}\right)-\frac{\delta_s^2}{E_{\rm W}^2}}\right], \tag{S6}$$

  which exist in the regime

$$\frac{\delta_{\rm s}}{E_{\rm W}}<1,\quad \frac{\chi N}{E_{\rm W}}>\frac{1}{\pi}. \tag{S7}$$

- Phase IIIa: Two pairs of complex roots with vanishing real parts,

$$\frac{u_1}{E_{\rm W}}=\pm\frac{i}{4}\left[\cot\left(\frac{E_{\rm W}}{\chi N}\right)+\sqrt{\csc^2\left(\frac{E_{\rm W}}{\chi N}\right)-\frac{\delta_s^2}{E_{\rm W}^2}}\right],\quad \frac{u_2}{E_{\rm W}}=\pm\frac{i}{4}\left[\cot\left(\frac{E_{\rm W}}{\chi N}\right)-\sqrt{\csc^2\left(\frac{E_{\rm W}}{\chi N}\right)-\frac{\delta_s^2}{E_{\rm W}^2}}\right], \tag{S8}$$

  which exist in the regime

$$\frac{\delta_{\rm s}}{E_{\rm W}}>1,\quad \frac{\chi N}{E_{\rm W}}>\frac{2}{\pi},\quad \frac{\delta_{\rm s}}{E_{\rm W}}<\csc\left(\frac{E_{\rm W}}{\chi N}\right). \tag{S9}$$

  In phase IIIa, the order parameter, $\Delta_{\rm BCS}$ oscillates around a non-zero value (non-ZOPA) as pointed out in Ref. [**? ?**].

- Phase IIIb: Two pairs of complex roots with non-zero real parts,

$$\frac{u_1}{E_{\rm W}}=\frac{1}{4}\left[\sqrt{\delta_s'^2-\csc^2\left(\frac{1}{\chi' N}\right)}\pm i\cot\left(\frac{1}{\chi' N}\right)\right],\quad \frac{u_2}{E_{\rm W}}=\frac{1}{4}\left[-\sqrt{\delta_s'^2-\csc^2\left(\frac{1}{\chi' N}\right)}\pm i\cot\left(\frac{1}{\chi' N}\right)\right], \tag{S10}$$

  which exist in the regime

$$\frac{\delta_{\rm s}}{E_{\rm W}}>1,\quad \frac{\chi N}{E_{\rm W}}>\frac{2}{\pi},\quad \frac{\delta_{\rm s}}{E_{\rm W}}>\csc\left(\frac{E_{\rm W}}{\chi N}\right). \tag{S11}$$

  In phase IIIb, $\Delta_{\rm BCS}$ oscillates with zero order parameter average (ZOPA) as explained in Ref. [**? ?**].

The dynamical phases derived from the Lax analysis above are supported by numerical evidences, as shown in Fig. S1**a** and Fig. S1**b**. We numerically solve the dynamics of $\Delta_{\rm BCS}=\chi\langle\hat{S}^-\rangle$ under Eq. (S1) based on mean field approximation, and then identify dynamical phases based on long-time average of $|\Delta_{\rm BCS}|$,

$$\mathrm{Avg}(|\Delta_{\rm BCS}|)=\lim_{T\to\infty}\frac{1}{T}\int_0^T|\Delta_{\rm BCS}(t)|dt, \tag{S12}$$

and long-time oscillation amplitude of $|\Delta_{\rm BCS}|$. Since the oscillations in $|\Delta_{\rm BCS}|$ might deviates from a sinusoidal form, it is easier to use the standard deviation as a measure of the oscillation amplitude,

$$\mathrm{Std}(|\Delta_{\rm BCS}|)=\left[\lim_{T\to\infty}\frac{1}{T}\int_0^T\Big(|\Delta_{\rm BCS}(t)|-\mathrm{Avg}(|\Delta_{\rm BCS}|)\Big)^2dt\right]^{1/2}, \tag{S13}$$

although experimentally it's better to use the peak of Fourier spectrum to suppress the noise (see Fig. 3**d** in the main text). The dynamical phases can be characterized by

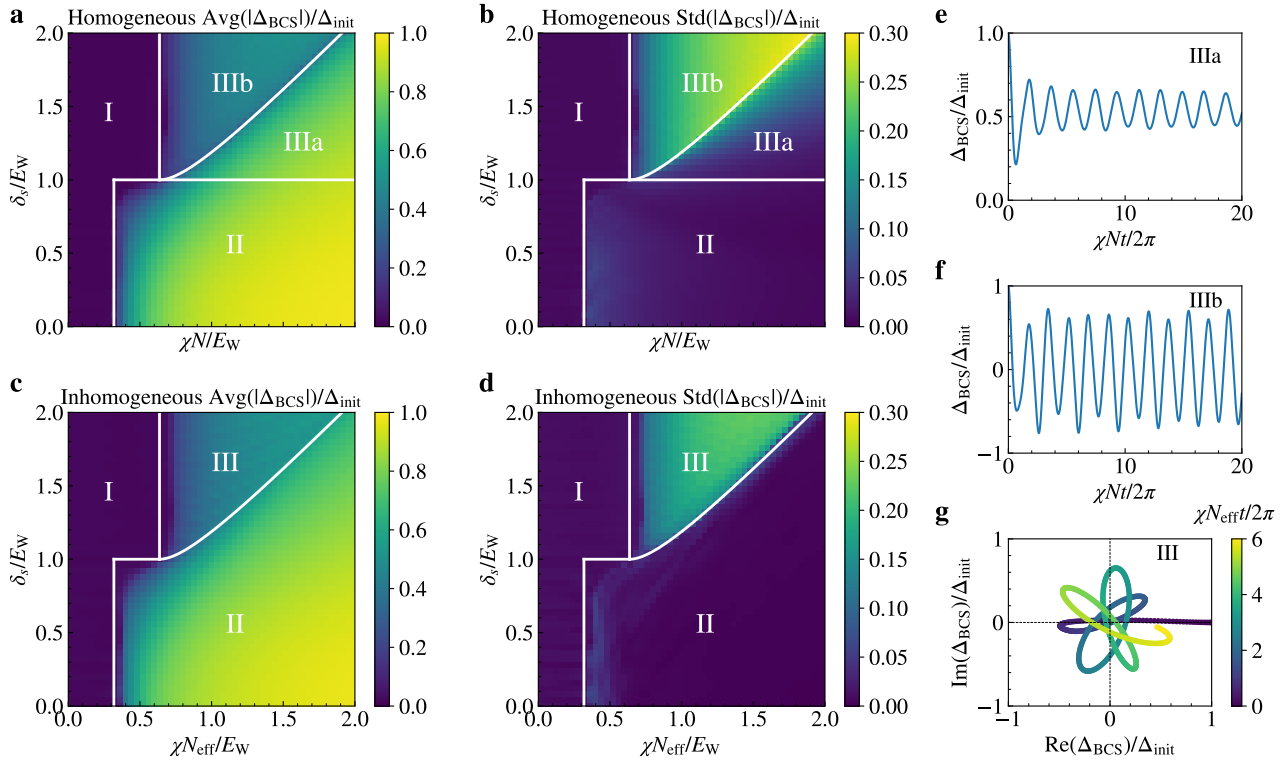

Fig. S1. **Dynamical phase diagrams.** **a** and **b**, Dynamical phase diagram of the homogeneous model normalized by $\Delta_{\rm init}/\chi N = 1/2$, where $\Delta_{\rm init}$ is the initial value of $|\Delta_{\rm BCS}|$. The white lines are the dynamical critical points derived from the Lax analysis. **c** and **d**, Dynamical phase diagram of the inhomogeneous model normalized by $\Delta_{\rm init}/\chi N_{\rm eff} = \mathcal{J}_1(\Omega\tau)$. The white lines are the same as the homogeneous model. **e**, Time evolution of $\Delta_{\rm BCS}$ at $\delta_{\rm s}/E_{\rm W} = 1.1$, $\chi N/E_{\rm W} = 1.0$ under the homogeneous model (phase IIIa). **f**, Time evolution of $\Delta_{\rm BCS}$ at $\delta_{\rm s}/E_{\rm W} = 1.6$, $\chi N/E_{\rm W} = 1.0$ under the homogeneous model (phase IIIb). **g**, Time evolution of $\Delta_{\rm BCS}$ at $\delta_{\rm s}/E_{\rm W} = 1.6$, $\chi N/E_{\rm W} = 1.0$ under the inhomogeneous model (phase III).

- Phase I: $\mathrm{Avg}(|\Delta_{\rm BCS}|) = 0$, $\mathrm{Std}(|\Delta_{\rm BCS}|) = 0$.
- Phase II: $\mathrm{Avg}(|\Delta_{\rm BCS}|) > 0$, $\mathrm{Std}(|\Delta_{\rm BCS}|) = 0$.
- Phase III: $\mathrm{Avg}(|\Delta_{\rm BCS}|) > 0$, $\mathrm{Std}(|\Delta_{\rm BCS}|) > 0$.

Since ε_k is chosen from a distribution with particle-hole symmetry (symmetric about 0), $\Delta_{\rm BCS}$ becomes a real number in this case. One can further separate phase IIIa and phase IIIb by the behavior of $\Delta_{\rm BCS}$ shown in Fig. S1**e** and Fig. S1**f**.

B. Inhomogeneous model

Here we discuss the dynamical phases for the BCS Hamiltonian with inhomogeneous coupling,

$$\hat{H} = \hbar\chi \sum_{jk} \zeta_j \zeta_k \hat{S}_j^+ \hat{S}_k^- + \sum_k \varepsilon_k \hat{S}_k^z, \tag{S14}$$

where ζ_k is generated by random sampling of $\cos(x)$, with x chosen from a uniform distribution in the interval $[0, 2\pi)$. Similar to the homogeneous model, $\varepsilon_k/\hbar$ is still chosen from a uniform distribution in the frequency range $[-\delta_{\rm s}/2 - E_{\rm W}/2, -\delta_{\rm s}/2 + E_{\rm W}/2]$ and $[\delta_{\rm s}/2 - E_{\rm W}/2, \delta_{\rm s}/2 + E_{\rm W}/2]$. In this case, we explore the dynamical phases numerically since the Lax analysis is not applicable. As shown in Fig. S3**c** and Fig. S3**d**, one can obtain similar dynamical phases as the homogeneous model: Phase I remains the same, Phase IIIa merges into Phase II, and Phase IIIb becomes the new Phase III. The phase boundary can be roughly captured by the analytical solution of the homogeneous model. Note that $\chi N_{\rm eff}$ is the averaged interaction strength in the inhomogeneous case, where $N_{\rm eff} = N/2$. The superconducting order parameter is defined as $\Delta_{\rm BCS} = \chi \sum_k \zeta_k \langle \hat{S}_k^- \rangle$. The initial condition is chosen

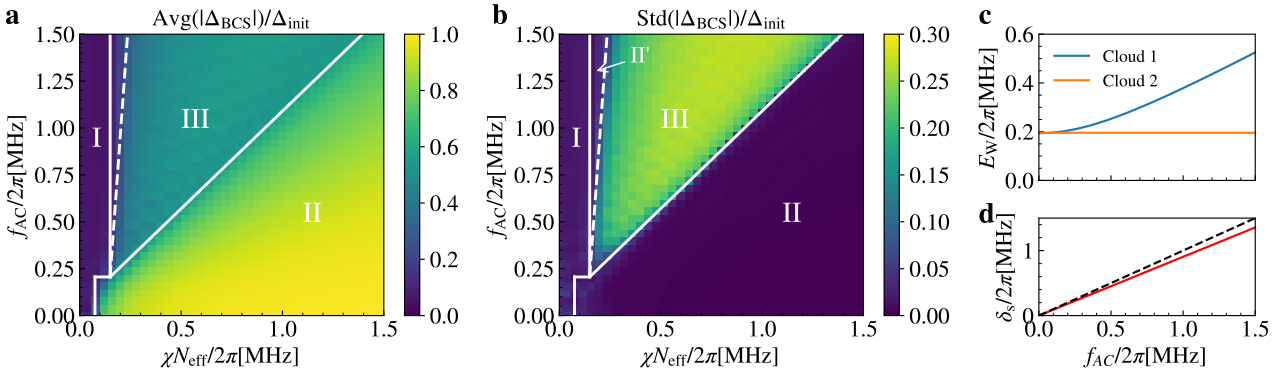

Fig. S2. **Experimental control of dynamical phases.** **a** and **b**, Dynamical phase diagram for the experiment with two atomic ensembles, in terms of averaged spin-exchange interaction strength $\chi N_{\rm eff}$ and peak AC Stark shift $f_{\rm AC}$. The white lines show the predicted dynamical phase boundaries to guide the eye. The white dashed line marks a small region of phase II' due to the imbalance of $E_{\rm W}$ for the two atomic ensembles. **c**, $E_{\rm W}$ as a function of peak AC Stark shift $f_{\rm AC}$, with AC Stark shift applying to atomic cloud 1. **d**, $\delta_{\rm s}$ as a function of peak AC Stark shift $f_{\rm AC}$ (red line). The dashed line marks the place where $\delta_{\rm s} = f_{\rm AC}$.

as the maximum $|\Delta_{\rm BCS}|$ one can achieved by an external drive along the cavity axis, $\hat{H}_{\rm drive} = \Omega \sum_k \zeta_k \hat{S}^y_k$. Assuming the initial state can be prepared by applying $\hat{H}_{\rm drive}$ for a time τ, we have

$$\frac{\Delta_{\rm init}}{\chi N_{\rm eff}} \approx \frac{1}{2\pi}\int_0^{2\pi} dx \cos(x)\sin(\Omega\tau\cos(x)) = \mathcal{J}_1(\Omega\tau), \tag{S15}$$

where $\mathcal{J}_n$ is the Bessel function of the first-kind, and the maximum of $\mathcal{J}_1(\Omega\tau)$ can be achieved at $\Omega\tau = 0.586\pi$. It is worth to mention that $\Delta_{\rm BCS}$ is a real number initially, but it becomes a complex number during the time evolution, as shown in Fig. S3**g**.

C. Experimental control of dynamical phases

Here we elaborate on the experimental implementation of the Hamiltonian Eq. (S14). As discussed in the previous section, we would like to approximately engineer single-particle energies $\varepsilon_k/\hbar$ sampled from a uniform distribution in the frequency range $[-\delta_{\rm s}/2 - E_{\rm W}/2, -\delta_{\rm s}/2 + E_{\rm W}/2]$ and $[\delta_{\rm s}/2 - E_{\rm W}/2, \delta_{\rm s}/2 + E_{\rm W}/2]$. The two different experimental schemes used in the main text to explore the energy distribution are summarized in the following table:

	Description	Approx. $\varepsilon_k/\hbar$
Scheme I (Fig. 2, main text)	1) Single atomic cloud 2) AC Stark shift	$[-\tilde{E}_{\rm W}/2, \tilde{E}_{\rm W}/2]$
Scheme II (Fig. 3, 4, main text)	1) Two atomic clouds 2) AC Stark shift to cloud 1	Cloud 1: $[-\delta_{\rm s}/2 - E_{\rm W}/2, -\delta_{\rm s}/2 + E_{\rm W}/2]$ Cloud 2: $[+\delta_{\rm s}/2 - E_{\rm W}/2, +\delta_{\rm s}/2 + E_{\rm W}/2]$

The first scheme is used to probe the phase I to phase II transition. We use a single atomic ensemble and apply an AC Stark shift beam with a gradient to approximately engineer $\varepsilon_k/\hbar$ from a uniform distribution $[-\tilde{E}_{\rm W}/2, \tilde{E}_{\rm W}/2]$, as discussed in the Methods. As shown in Fig. 2**a** in the main text, the distribution of atomic frequencies is not exactly uniform, so we calculate the variance of the frequency distribution experimentally. Theoretically we assign a spread $\tilde{E}_{\rm W}$ such that the uniform distibution over $[-\tilde{E}_{\rm W}/2, \tilde{E}_{\rm W}/2]$ matches the measured experimental variance. We use this scheme to probe the dynamical phase diagram at $\delta_{\rm s} = 0$ (see Fig. 1**c** in the main text).

It is worth mentioning that the uniform distribution $[-\tilde{E}_{\rm W}/2, \tilde{E}_{\rm W}/2]$ can be interpreted in two different ways: 1) $\delta_{\rm s} = 0$ and $E_{\rm W} = \tilde{E}_{\rm W}$; 2) $\delta_{\rm s} = E_{\rm W} = \tilde{E}_{\rm W}/2$. Here we prefer the first interpretation $\delta_{\rm s} = 0$ because in this scheme we only have a single control parameter (the strength of AC Stark shift beam). Additionally, the line $\delta_{\rm s} = E_{\rm W}$ in the dynamical phase diagram has an implication that a small perturbation of $\delta_{\rm s}$ can generate a gap in atomic frequency, which is prohibited under this mapping between experimental controls and the model parameters.

In the second scheme that probes transitions into phase III, we use two atomic ensembles and apply an AC Stark shift beam (peak AC Stark shift $f_{\rm AC}$) to the first ensemble to generate a frequency splitting $\delta_{\rm s}$ between the two

ensembles. In contrast to the first scheme, as discussed in the Methods, here we instead use the differential lattice light shifts to engineer a frequency spread E_{W} for each ensemble. As shown in Fig. 3**a** in the main text, in this case we define δ_{s} as the mean frequency difference between the two ensembles, and E_{W} as the width of a uniform distribution generating the same variance.

It is worth mentioning that the Gaussian profile of the AC Stark shift beam leads to an increase in E_{W} for the first atomic ensemble, as well as a reduction of the expected splitting of the two ensembles $\delta_{\mathrm{s}} < f_{\mathrm{AC}}$, as shown in Fig. S2**c** and **d**. Using experimental parameters, we get the dynamical phase diagram as depicted in Fig. S2**a** and **b**. The imbalance of E_{W} for the two atomic ensembles can lead to a small region of phase II' marked by the white dashed line. This occurs because the spin-exchange interaction is able to lock the ensemble with smaller E_{W}, while the ensemble with larger E_{W} remains unlocked, which leads to $|\Delta_{\mathrm{BCS}}|$ approaching a small but nonzero constant value. In the experiment, due to other dissipative processes and reduced signal-to-noise ratio for small χN, we do not observe a difference between phase I and phase II'. This is the cause of a small discrepancy between theory and experiment in Fig. 4**b** in the main text in identifying the position of the phase transition.

S2. SHORT-TIME SIGNATURES OF DYNAMICAL PHASES

In this section, we discuss the properties of the dynamical phases using short-time observables, since dissipative processes and noise in the experiment lead to difficulties in measuring long-time observables. In the following, we show that phase I can be characterized by the fast decay of $|\Delta_{\mathrm{BCS}}|$, phase II can be characterized by Higgs oscillations. We further show that the phase II to phase III transition can be captured by the dip in the short-time oscillation frequency of $|\Delta_{\mathrm{BCS}}|$. Finally, we provide an explanation of the frequency dip using an analytical solution of the two-spin BCS model.

A. Phase I: fast decay

In phase I, the single-particle energy term $\sum_k \varepsilon_k \hat{S}_k^z$ dominates over the spin-exchange interaction. To leading order, one can calculate $|\Delta_{\mathrm{BCS}}|$ in the homogeneous model by dropping the interaction term, which gives

$$\begin{aligned}\frac{|\Delta_{\mathrm{BCS}}|}{\chi N} &\approx \frac{1}{2N}\Big|\sum_k e^{-i\varepsilon_k t/\hbar}\Big| = \frac{1}{2}\Big|\frac{1}{2E_{\mathrm{W}}}\int_{-\delta_{\mathrm{s}}/2-E_{\mathrm{W}}/2}^{-\delta_{\mathrm{s}}/2+E_{\mathrm{W}}/2} e^{-ixt}dx + \frac{1}{2E_{\mathrm{W}}}\int_{\delta_{\mathrm{s}}/2-E_{\mathrm{W}}/2}^{\delta_{\mathrm{s}}/2+E_{\mathrm{W}}/2} e^{-ixt}dx\Big| \\ &= \frac{1}{2}\Big|\cos\left(\frac{\delta_{\mathrm{s}}}{2}\right)\Big| \cdot \Big|\frac{\sin(E_{\mathrm{W}}t/2)}{E_{\mathrm{W}}t/2}\Big|.\end{aligned} \tag{S16}$$

The decay profile of $|\Delta_{\mathrm{BCS}}|$ is set by a sinc function with a $1/e$ coherence time t satisfying $E_{\mathrm{W}}t/2\pi \approx 0.7$. For the inhomogeneous model a similar fast decay time scale of the order of $E_{\mathrm{W}}t/2\pi \sim 1$ can be derived. As shown in Fig. 2**b** in the main text, we observe fast decay of $|\Delta_{\mathrm{BCS}}|$ within 1 μs in phase I. The decay time scale for the other dynamical phases can be more than 10 times longer.

B. Phase II: Higgs oscillation

Higgs oscillation, generated by collective excitation of the Higgs mode in BCS superconductor, is characterized by the oscillation of $|\Delta_{\mathrm{BCS}}|$ at frequency $\omega = 2\mathrm{Avg}(|\Delta_{\mathrm{BCS}}|)$ [**?**]. For the homogeneous model (see Fig. S3**a**), we numerically confirmed this relation for all the points in phase II and phase IIIa. For the inhomogeneous model (see Fig. S3**b**), this relation is approximately satisfied in phase II. In experiment, we observe hints of Higgs oscillation (see Fig. 2 in the main text), which can be ideally described by the inhomogeneous model with $\delta_{\mathrm{s}} = 0$ (see the inset in Fig. S3**b**).

C. Transition to phase III: frequency dip

In the main text, we discuss a way to understand the phase II to phase III transition by visualising the two atomic ensembles as two large spins. For the inhomogeneous model, phase II exists in the small δ_{s} regime, where the two spins lock to each other and form a single large spin through spin-exchange interactions. In this case the many-body gap protection leads to the damped oscillations observed in phase II. Increasing δ_{s} in phase II leads to the reduction

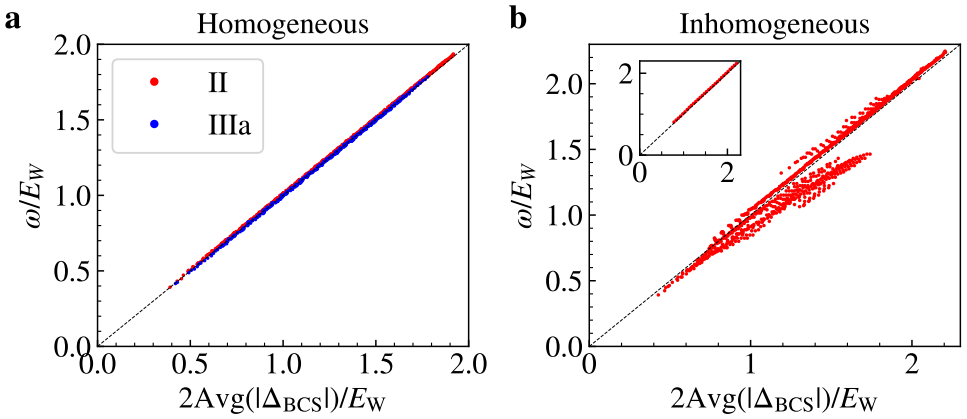

Fig. S3. **Relation between oscillation frequency and averaged order parameter in Higgs oscillations. a**, Homogeneous model where each point is a choice of $(\chi N, \delta_{\mathrm{s}})$ in phase II (red) and phase IIIa (blue). The dashed line represents $\omega = 2\mathrm{Avg}(|\Delta_{\mathrm{BCS}}|)$. **b**, Inhomogeneous model where each point is a choice of $(\chi N_{\mathrm{eff}}, \delta_{\mathrm{s}})$ in phase II. The inset shows the points with $\delta_{\mathrm{s}} = 0$.

of the many-body gap, and hence to a decrease of the corresponding oscillation frequency. Phase III exists in the large δ_{s} regime, where the spin locking occurs separately in each ensemble, and the two large spin are instead precessing around each other, with a rate set by the splitting δ_{s} and the spin-exchange interaction. Increasing δ_{s} in phase III leads to a speed up of the oscillation frequency. Therefore one expects the existence of a frequency dip separating between phase II and phase III. Indeed as shown in Fig. S4**c** and **d**, we find good agreement between the frequency dip and the corresponding dynamical critical point. For small δ_{s}, the oscillation frequency approaches the Higgs oscillation frequency discussed in the previous subsection. For large δ_{s}, the oscillation frequency approaches δ_{s}. The reduction of oscillation frequency compared to δ_{s} indicates many-body effects in phase III. It's worth to mention that in contrast to the inhomogeneous model, the frequency dip indicates the phase IIIa to phase IIIb transition for the homogeneous model.

D. Frequency dip in the two-spin BCS model

Here we use the analytical mean field solution of the BCS Hamiltonian with two large spins ($S = N/4$ for each spin) to understand the frequency dip discussed above. In this case, the Hamiltonian simplifies to

$$\hat{H}/\hbar = \chi \hat{S}^+ \hat{S}^- + \frac{\delta_{\mathrm{s}}}{2}\hat{S}_1^z - \frac{\delta_{\mathrm{s}}}{2}\hat{S}_2^z, \tag{S17}$$

where $\hat{S}^{\pm} = \hat{S}_1^{\pm} + \hat{S}_2^{\pm}$. The mean field equations of motion for the Hamiltonian above can then be written as

$$\begin{aligned}
&\frac{d}{dt}S_1^x = 2\chi S^y S_1^z - \frac{\delta_{\mathrm{s}}}{2}S_1^y, \quad \frac{d}{dt}S_1^y = -2\chi S^x S_1^z + \frac{\delta_{\mathrm{s}}}{2}S_1^x, \quad \frac{d}{dt}S_1^z = -2\chi(S_2^y S_1^x - S_2^x S_1^y),\\
&\frac{d}{dt}S_2^x = 2\chi S^y S_2^z + \frac{\delta_{\mathrm{s}}}{2}S_2^y, \quad \frac{d}{dt}S_2^y = -2\chi S^x S_2^z - \frac{\delta_{\mathrm{s}}}{2}S_2^x, \quad \frac{d}{dt}S_2^z = -2\chi(S_1^y S_2^x - S_1^x S_2^y).
\end{aligned} \tag{S18}$$

The spin components without the hat represent the expectation value of the corresponding spin operators.

In the following, we assume an initial state satisfying $S_1^x = S_2^x = N/4$, $S_1^y = S_2^y = S_1^z = S_2^z = 0$. The conserved quantities of the two-spin BCS model are the total magnetisation

$$S^z = S_1^z + S_2^z = 0, \tag{S19}$$

the total energy

$$E/\hbar = \chi S^+ S^- + \frac{\delta_{\mathrm{s}}}{2}S_1^z - \frac{\delta_{\mathrm{s}}}{2}S_2^z = \chi\left(\frac{N}{2}\right)^2, \tag{S20}$$

as well as the spin length of each of the large spins, $(S_1^x)^2 + (S_1^y)^2 + (S_1^z)^2 = (N/4)^2$, $(S_2^x)^2 + (S_2^y)^2 + (S_2^z)^2 = (N/4)^2$. Using these conserved quantities, one can derive from the mean field equations in Eq. (S18) an equation of motion for

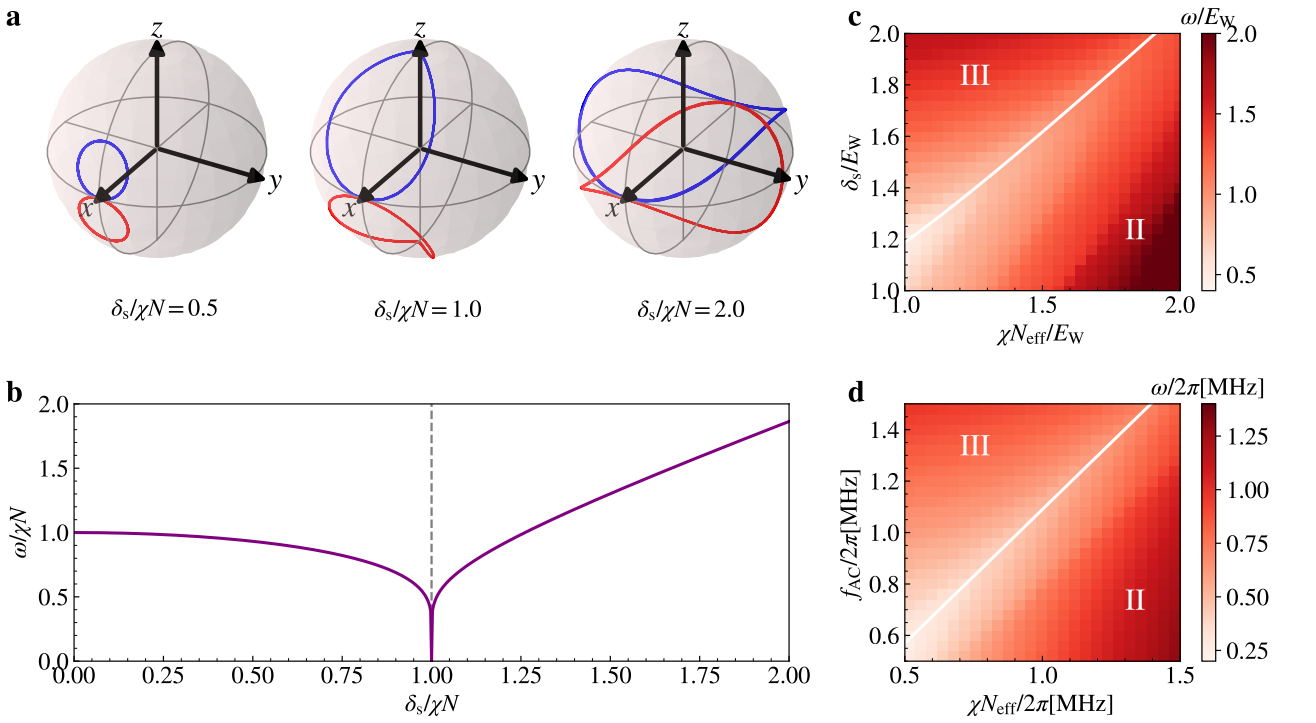

Fig. S4. **Frequency dip as a signature of the phase II to phase III transition.** **a**, Mean field trajectories of the two large spin model evolving under Eq. (S17). From left to right, Bloch spheres display trajectories with $\delta_s/(\chi N) = 0.5, 1$, and 2 respectively. **b**, Oscillation frequency of $|\Delta_{BCS}|$ in the two-spin BCS model Eq. (S17) as a function of $\delta_s/\chi N$. The frequency dip at $\delta_s/\chi N = 1$ marks the dynamical phase transition point. **c**, Short-time frequency ω of the dynamics under inhomogeneous atom-light coupling (see Eq. (3) in the Methods). The white line marks the phase II to phase III transition, the same boundary as shown in Extended Data Fig. 2 from the Methods. **d**, Short-time frequency ω of the dynamics using experimental control parameters. The white line marks the phase II to phase III transition and represents the same boundary as in Fig. S2. The frequency dips match the dynamical critical points for both cases.

the BCS order parameter, $\Delta_{BCS} = \chi S^-$. To simplify the notation, we define $\Delta \equiv |\Delta_{BCS}|/\chi N$, i.e. $\Delta^2 = S^+S^-/N^2$. From Eq. (S19) and Eq. (S20), we obtain

$$\frac{d}{dt}\Delta^2 = -\frac{\delta_s}{\chi N^2}\frac{d}{dt}S_1^z = \frac{2\delta_s}{N^2}(S_2^yS_1^x - S_2^xS_1^y), \tag{S21}$$

which leads to

$$\begin{aligned}\frac{d^2}{dt^2}\Delta^2 &= \frac{2\delta_s}{N^2}\left(S_1^x\frac{d}{dt}S_2^y + S_2^y\frac{d}{dt}S_1^x - S_1^y\frac{d}{dt}S_2^x - S_2^x\frac{d}{dt}S_1^y\right)\\ &= 4\delta_s\chi\Delta^2S_1^z - \frac{2\delta_s^2}{N^2}(S_1^xS_2^x + S_1^yS_2^y).\end{aligned} \tag{S22}$$

From the above conserved quantities, we can create the equivalent expressions $\delta_sS_1^z = -\chi N^2(\Delta^2 - 1/4)$, $2(S_1^xS_2^x + S_1^yS_2^y) = N^2\Delta^2 - 2\times(N/4)^2 + 2(S_1^z)^2$. Plugging these into the equation of motion gives

$$\frac{d^2}{dt^2}\Delta^2 = -6(\chi N)^2(\Delta^2)^2 + \left(2(\chi N)^2 - \delta_s^2\right)\Delta^2 + \frac{\delta_s^2 - (\chi N)^2}{8}. \tag{S23}$$

The equation above can be further simplified to

$$\frac{1}{2}\left(\frac{d}{dt}\Delta\right)^2 + V(\Delta) = 0, \tag{S24}$$

where

$$V(\Delta) = \frac{1}{2}(\chi N)^2\left(\Delta^2 - \frac{1}{4}\right)\left(\Delta^2 - \frac{1-(\delta_s/\chi N)^2}{4}\right), \tag{S25}$$

with an initial condition $\Delta = 1/2$. Eq. (S24) can be understood as a classical particle with position Δ oscillating in the potential $V(\Delta)$. For $\delta_s < \chi N$, we find Δ oscillating between $\Delta_{\max} = 1/2$ and $\Delta_{\min} = \sqrt{1-(\delta_s/\chi N)^2}/2$. This is equivalent to phase II in the cases of many spins with inhomogeneous atom-light couplings, because all the oscillations damp in the large χN limit. For $\delta_s > \chi N$, we find Δ oscillating between $\Delta_{\max} = 1/2$ and $\Delta_{\min} = 0$, since the definition of Δ requires $\Delta \geq 0$. This is equivalent to phase III in the cases of many spins because the phase connects to single-particle oscillations in the large δ_s limit. Therefore, a dynamical phase transition occurs at $\delta_s/\chi N = 1$, which is equivalent to the phase II to phase III transition in the many-spin system.

The analytical solution of Eq. (S24) can be written in terms of Jacobian elliptic funtions dn and cn:

$$\Delta(t) = \begin{cases} \frac{1}{2}\mathrm{dn}\left(\frac{1}{2}\chi N t \middle| (\delta_s/\chi N)^2\right) & \text{if } \delta_s < \chi N \\ \\ \frac{1}{2}\left|\mathrm{cn}\left(\frac{1}{2}\delta_s t \middle| (\chi N/\delta_s)^2\right)\right| & \text{if } \delta_s > \chi N \end{cases}. \tag{S26}$$

The frequency of $\Delta(t)$ can be written in terms of the complete elliptic integral of the first kind $K(k^2)$:

$$\frac{\omega}{\chi N} = \begin{cases} \frac{\pi}{2K\left((\delta_s/\chi N)^2\right)} & \text{if } \delta_s < \chi N \\ \\ \frac{\delta_s}{\chi N}\frac{\pi}{2K\left((\chi N/\delta_s)^2\right)} & \text{if } \delta_s > \chi N \end{cases}. \tag{S27}$$

The mean-field trajectories on the Bloch sphere are shown in Fig. S4**a**, and the oscillation frequency Eq. (S27) is shown in Fig. S4**b**. The dynamical phase transition can also be understood from the mean field trajectories. For $\delta_s < \chi N$, the two large spins lock to each other and oscillate near the x axis of the Bloch sphere. For $\delta_s > \chi N$, the two large spins are unlocked and precess around the whole Bloch sphere. Near the dynamical critical point, the mean field trajectories are close to the north pole or south pole of the Bloch sphere, which leads to a slow down of the oscillations because they approach stable fixed points of the Hamiltonian.

S3. AXIAL MOTION

In this section, we elaborate on how to take into account axial motion present in the experimental system. Similar discussions can be found in Ref. [**?**]. We start with the one-dimensional Hamiltonian of our cavity QED system with two internal atomic levels ($|\uparrow\rangle$ and $|\downarrow\rangle$), given by

$$\begin{aligned} \hat{H} = &\sum_{\sigma=\{\uparrow,\downarrow\}} \int dx\ \hat{\psi}^\dagger_\sigma(x)\left[\frac{\hat{p}^2}{2M} + V_0\sin^2(k_L x)\right]\hat{\psi}_\sigma(x) + \int dx\ \hat{\psi}^\dagger_\uparrow(x)\left[\hbar\omega_0 + U_{ac}(x)\right]\hat{\psi}_\uparrow(x) \\ &+ \hbar g_c \int dx\ \cos(k_c x)\left[\hat{\psi}^\dagger_\uparrow(x)\hat{\psi}_\downarrow(x)\hat{a} + \hat{a}^\dagger\hat{\psi}^\dagger_\downarrow(x)\hat{\psi}_\uparrow(x)\right] + \hbar\omega_c\hat{a}^\dagger\hat{a}, \end{aligned} \tag{S28}$$

where $k_L = 2\pi/\lambda_L$ is the wavenumber of the lattice beams ($\lambda_L = 813$nm), k_c is the wavenumber of the cavity mode ($\lambda_c = 689$nm), ω_0 is the atomic transition frequency between $|\uparrow\rangle$ and $|\downarrow\rangle$ states, $U_{ac}(x)$ is the AC Stark shift applied to the atoms (including the differential light shift from the lattice beams and the transverse AC Stark shift beam), and ω_c is the frequency of cavity resonance.

Since the atoms are trapped in an optical lattice with lattice depth on the order of $10^3 E_R$, we can approximate each lattice site as an harmonic trap with axial trapping frequency $\hbar\omega_T = \sqrt{4V_0 E_R}$, where $E_R = \hbar^2 k_L^2/2M$ is the lattice recoil energy. We also ignore tunnelling processes between lattice sites. In this case, one can expand the atomic field operator in terms of lattice site index j and harmonic oscillator levels n:

$$\hat{\psi}_\sigma(x) = \sum_{jn} \hat{c}_{jn,\sigma}\phi_n(x - ja_L). \tag{S29}$$

Here, $a_L = \lambda_L/2$ is the lattice spacing, and ϕ_n is the harmonic oscillator wave function for mode n, given by

$$\phi_n(x) = \frac{1}{\sqrt{2^n n!}}\left(\frac{M\omega_T}{\pi\hbar}\right)^{1/4} \mathrm{e}^{-M\omega_T x^2/2\hbar} H_n\left(\sqrt{\frac{M\omega_T}{\hbar}}x\right) \tag{S30}$$

where $H_n(x)$ are the Hermite polynomials. Plugging this expansion into the Hamiltonian and transforming to the rotating frame of the atoms, we obtain

$$\hat{H}/\hbar = \sum_{jn\sigma} n\omega_T \hat{c}^\dagger_{jn,\sigma}\hat{c}_{jn,\sigma} + \sum_{jn} \varepsilon_{jn}\hat{c}^\dagger_{jn,\uparrow}\hat{c}_{jn,\uparrow} + g_c \sum_{jnm} \zeta^{nm}_j (\hat{c}^\dagger_{jn,\uparrow}\hat{c}_{jm,\downarrow}\hat{a} + \hat{a}^\dagger \hat{c}^\dagger_{jm,\downarrow}\hat{c}_{jn,\uparrow}) + \delta_c \hat{a}^\dagger\hat{a} \tag{S31}$$

where $\delta_c = \omega_c - \omega_a$. For simplicity, we assume $U_{ac}(x)$ is either small or slowly varying in space and thus does not change the trap geometry. This term gives rise to an inhomogeneous transition frequency $\varepsilon_{jn} = \int dx U_{ac}(x)[\phi_n(x - ja_L)]^2/\hbar$. We calculate ζ^{nm}_j in the following way:

$$\begin{aligned}
\zeta^{nm}_j &= \int dx\ \cos(k_c x)\phi_n(x - ja_L)\phi_m(x - ja_L) = \int dx\ \cos(k_c x + k_c j a_L)\phi_n(x)\phi_m(x) \\
&= \cos(j\varphi)\int dx\ \cos(k_c x)\phi_n(x)\phi_m(x) - \sin(j\varphi)\int dx\ \sin(k_c x)\phi_n(x)\phi_m(x) \\
&= \cos(j\varphi)\,\mathrm{Re}\left[(i\eta)^s e^{-\eta^2/2}\sqrt{\frac{n_<!}{n_>!}}L^s_{n_<}(\eta^2)\right] - \sin(j\varphi)\,\mathrm{Im}\left[(i\eta)^s e^{-\eta^2/2}\sqrt{\frac{n_<!}{n_>!}}L^s_{n_<}(\eta^2)\right].
\end{aligned} \tag{S32}$$

where $\varphi = \pi k_L/k_c$, $s = |n - m|$, $n_< = \min(n, m)$, $n_> = \max(n, m)$, $L^\alpha_n(x)$ are the generalised Laguerre polynomials, and $\eta = k_c\sqrt{\hbar/2M\omega_T}$ is the Lamb-Dicke parameter. In our case $\omega_T/2\pi = 165$ kHz, implying that $\eta = 0.17$. This places us in the Lamb-Dicke regime where ζ^{nm}_j is negligible for $|n - m| > 1$. It can be convenient to rewrite the Hamiltonian in terms of operators $\hat{S}^j_{n\sigma,m\sigma'} = \hat{c}^\dagger_{jn,\sigma}\hat{c}_{jm,\sigma'}$, resulting in the following form:

$$\hat{H}/\hbar = \sum_{jn\sigma} n\omega_T \hat{S}^j_{n\sigma,n\sigma} + \sum_{jn} \varepsilon_{jn}\hat{S}^j_{n\uparrow,n\uparrow} + g_c \sum_{jnm} \zeta^{nm}_j (\hat{S}^j_{n\uparrow,m\downarrow}\hat{a} + \hat{a}^\dagger \hat{S}^j_{m\downarrow,n\uparrow}) + \delta_c \hat{a}^\dagger\hat{a}. \tag{S33}$$

In addition to the Hamiltonian dynamics, we also consider dissipation processes such as cavity loss with a rate $\kappa/2\pi = 153$ kHz, as well as spontaneous emission with a rate $\gamma/2\pi = 7.5$ kHz. The full dynamics of this open system can be described by the following Lindblad master equation:

$$\frac{\mathrm{d}}{\mathrm{d}t}\hat{\rho} = -\frac{i}{\hbar}[\hat{H}, \hat{\rho}] + \left[\hat{L}_{\mathrm{cav}}\hat{\rho}\hat{L}^\dagger_{\mathrm{cav}} - \frac{1}{2}\{\hat{L}^\dagger_{\mathrm{cav}}\hat{L}_{\mathrm{cav}}, \hat{\rho}\}\right] + \sum_{jn}\left[\hat{L}_{j,n}\hat{\rho}\hat{L}^\dagger_{j,n} - \frac{1}{2}\{\hat{L}^\dagger_{j,n}\hat{L}_{j,n}, \hat{\rho}\}\right], \tag{S34}$$

where the jump operator for cavity loss is given by $\hat{L}_{\mathrm{cav}} = \sqrt{\kappa}\hat{a}$, and the single-particle jump operators for spontaneous emission are given by $\hat{L}_{j,n} = \sqrt{\gamma}\hat{S}^j_{n\downarrow,n\uparrow}$. Here, we assume that spontaneous emission is in the Lamb-Dicke regime.

In the experiment, δ_c is the largest frequency scale ($\delta_c \gg g_c\sqrt{N}, \kappa$), so we can adiabatically eliminate the cavity photons [**?**] and obtain the following effective atom-only master equation:

$$\frac{\mathrm{d}}{\mathrm{d}t}\hat{\rho} = -\frac{i}{\hbar}[\hat{H}_{\mathrm{eff}}, \hat{\rho}] + \left[\hat{L}_{\mathrm{col}}\hat{\rho}\hat{L}^\dagger_{\mathrm{col}} - \frac{1}{2}\{\hat{L}^\dagger_{\mathrm{col}}\hat{L}_{\mathrm{col}}, \hat{\rho}\}\right] + \sum_{jn}\left[\hat{L}_{j,n}\hat{\rho}\hat{L}^\dagger_{j,n} - \frac{1}{2}\{\hat{L}^\dagger_{j,n}\hat{L}_{j,n}, \hat{\rho}\}\right]. \tag{S35}$$

Here, the effective Hamiltonian is given by

$$\hat{H}_{\mathrm{eff}}/\hbar = \sum_{jn\sigma} n\omega_T \hat{S}^j_{n\sigma,n\sigma} + \sum_{jn} \varepsilon_{jn}\hat{S}^j_{n\uparrow,n\uparrow} + \chi \sum_{jnm}\sum_{kpq} \zeta^{nm}_j \zeta^{pq}_k \hat{S}^j_{n\uparrow,m\downarrow}\hat{S}^k_{p\downarrow,q\uparrow}, \tag{S36}$$

and effective collective jump operator generating superradiant decay takes the form

$$\hat{L}_{\mathrm{col}} = \sqrt{\Gamma}\sum_{jnm} \zeta^{nm}_j \hat{S}^j_{m\downarrow,n\uparrow}, \tag{S37}$$

where $\chi = -g_c^2\delta_c/(\delta_c^2 + \kappa^2/4)$ and $\Gamma = g_c^2\kappa/(\delta_c^2 + \kappa^2/4)$. The equivalent superconducting order parameter takes the following form:

$$\Delta_{\mathrm{BCS}} = \chi \sum_{kpq} \zeta^{pq}_k \langle \hat{S}^k_{p\downarrow,q\uparrow}\rangle. \tag{S38}$$

One can recover the inhomogeneous model discussed in the previous section by removing the axial harmonic oscillator level labels.

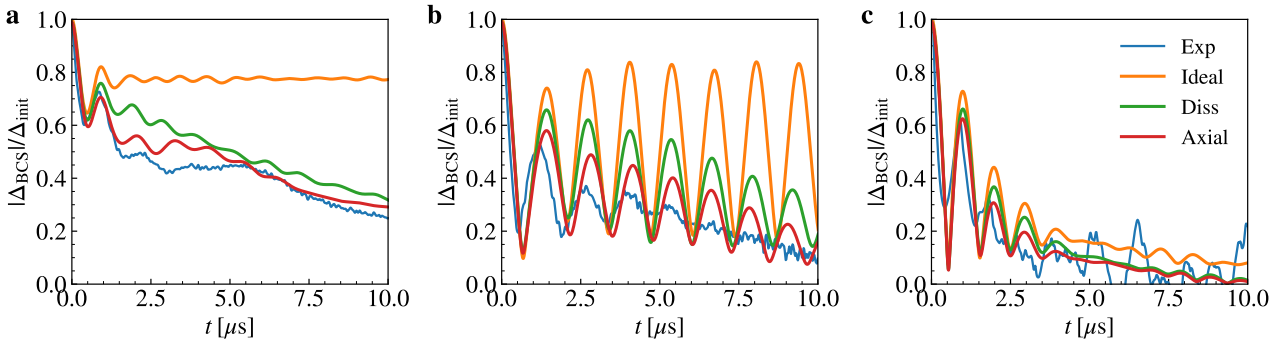

Fig. S5. **Understanding experimental results with axial motion effects.** **a** Example phase II traces with $\chi N/2\pi = 1.29$MHz, $f_{AC}/2\pi = 1.1$MHz. **b** Example phase III traces with $\chi N/2\pi = 0.79$MHz, $f_{AC}/2\pi = 1.1$MHz. **c** Example phase I traces with $\chi N/2\pi = 0.15$MHz, $f_{AC}/2\pi = 1.1$MHz. The blue points are experimental data, the orange lines represent numerical simulations under ideal conditions (see Eq. (3) in the Methods), the green lines include dissipative processes on top of the ideal simulations, and the red lines consider both dissipative processes and axial motion effects.

Similarly, the Hamiltonian for initial state preparation takes the form

$$\hat{H}_{\text{drive}}/\hbar = \sum_{jn\sigma} n\omega_T \hat{S}^j_{n\sigma,n\sigma} + \frac{1}{2}\sum_{jnm} \zeta_j^{nm}(\Omega \hat{S}^j_{n\uparrow,m\downarrow} + \Omega^* \hat{S}^j_{m\downarrow,n\uparrow}). \tag{S39}$$

In numerical simulations, we perform a mean-field approximation, which replaces the operators $\hat{S}^j_{p\sigma,q\sigma'}$ by their expectation values $\langle \hat{S}^j_{p\sigma,q\sigma'} \rangle$ in the Heisenberg equation of motion. We perform a random sampling of the axial harmonic oscillator mode n for each atom based on a thermal distribution of 15 μK, and we only include the modes n and $n \pm 1$ into our calculation due to the Lamb-Dicke parameter. The atom number in our simulations is set to 2000; to match χN to experimental values, we rescale χ accordingly. We also empirically take into account two additional dissipation processes to quantitatively capture the behavior of $|\Delta_{BCS}|$ at longer time scales. The first is a single-particle decoherence between electronic states, described by the jump operators $\hat{L}^{\text{el}}_{j,\sigma} = \sqrt{\gamma_{\text{el}}} \sum_n \hat{S}^j_{n\sigma,n\sigma}$ with $\gamma_{\text{el}}/2\pi < 1$kHz for Fig. 2 starting from $t = 0\mu$s, and by $\gamma_{\text{el}}/2\pi = 0.0036(f_{AC}/2\pi) + 4$kHz for Fig. 3 and Fig. 4 in the main text. The second is a single-particle decoherence between motional states, described by the jump operators $\hat{L}^{\text{mo}}_{j,n} = \sqrt{\gamma_{\text{mo}}} \sum_\sigma \hat{S}^j_{n\sigma,n\sigma}$ with $\gamma_{\text{mo}}/2\pi = 15$kHz.

Some example traces including axial motion effects are depicted in Fig. S5. Generally speaking, accounting for these effects allows us to more accurately predict features present in the experimentally measured evolution of $|\Delta_{BCS}|$, at the same time leaving the predicted dynamical phase boundaries unchanged. As shown in Fig. S5a, including axial motion effects in phase II traces allows us to capture the faster damping rate of the Higgs oscillations, as well as a slow oscillation in $|\Delta_{BCS}|$ at the axial trapping frequency. Likewise, as shown in Fig. S5b, including axial motion effects in phase III traces allows us to capture the faster damping rate of the oscillations in $|\Delta_{BCS}|$, although the observed damping rate is still faster than the rate predicted by theory. Finally, as shown in Fig. S5c, all the theory simulations of phase I dynamics are similar to the simulation under ideal conditions, indicating that axial motion does not play an significant role in this regime.